Sensors and Materials, Vol. 38, No. 4 (2026) 1787–1802
MYU Tokyo

S & M 4406

Wearable Sweat Sodium Ion Biosensor for Personalized Hydration Strategy under Exercise-Induced Heat Stress

Shuai Zhang[1*] and Yong Zhang[2]

[1]Liaoning Equipment Manufacture College of Vocational Technology, Shenyang, Liaoning 110165, China
[2]Wuhan Polytechnic University, Wuhan, Hubei 430000, China,

(Received December 10, 2025; accepted February 24, 2026)

Keywords: electrochemical sensing, ion-selective membrane, carbon nanotube composite, wearable platform, hydration monitoring

A flexible, screen-printed potentiometric biosensor was developed for the continuous, noninvasive monitoring of sodium concentration in human sweat. The sensor employed a poly(vinyl chloride) membrane doped with sodium ionophore X and sodium tetrakis[3,5-bis(trifluoromethyl)phenyl]borate, with multiwalled carbon nanotubes (MWCNTs, 0–1 wt%) incorporated to enhance ion-to-electron transduction. Structural characterization by scanning electron microscopy (SEM), X-ray diffraction (XRD), and X-ray photoelectron Spectroscopy (XPS) confirmed homogeneous membrane formation and effective nanotube integration. Electrochemical analysis revealed a progressive improvement in performance with MWCNT loading: the sensitivity increased from 45.5 ± 1.2 to 58.2 ± 0.7 mV dec^{-1}, the detection limit decreased to 9.1 × 10^{-5} M, and the potential drift was minimized to 0.1 mV h^{-1}. The optimized device responded within 10 s and maintained stable slopes after 5000 bending and 2000 stretching cycles, demonstrating strong mechanical durability. Selectivity coefficients (log $K_{Na,j}^{pot} \approx -2.5$ to -3.4) confirmed negligible interference from K^+, NH_4^+, Ca^{2+}, and Mg^{2+}. During on-body trials involving 10 subjects performing 60 min of cycling at 27 °C, the wearable sensor accurately captured dynamic sweat Na^+ profiles ranging from 45 to 70 mM. Sensor readings correlated excellently with ion-chromatography reference values ($R^2 = 0.985$, mean bias –1.2 mM). These results validate the device as a reliable real-time platform for individualized fluid-electrolyte assessment. The integration of nanocomposite solid-contact membranes with flexible printed electronics enables the precise quantification of sweat electrolytes, supporting data-driven, personalized hydration management during exercise and heat exposure.

1. Introduction

Muscular exercise, particularly when performed in hot environments, imposes significant physiological strain on the human body. The metabolic rate can increase by 5 to 15 times the resting rate, with 70 to 100% of this energy released as heat that must be dissipated to maintain thermal homeostasis.(1) The primary mechanism for this thermoregulation is sweating, a process

*Corresponding author: e-mail: 03021622@163.com
https://doi.org/10.18494/SAM6107

ISSN 0914-4935

governed by the autonomic nervous system. During intense physical activity or in warm climates, sweat rates can be substantial, commonly ranging from 1.0 to 2.5 $L \cdot h^{-1}$.(2) This high rate of fluid loss often exceeds voluntary fluid intake, leading to a state of hypohydration, or body water deficit. Hypohydration affects both intracellular and extracellular fluid compartments, resulting in decreased plasma volume and a concomitant increase in plasma osmolality. This physiological disruption significantly impairs athletic performance by increasing heat storage, reducing aerobic capacity, and negating the thermoregulatory advantages conferred by physical fitness and heat acclimation.

A critical component of this physiological challenge is the loss of electrolytes, of which sodium (Na^+) is the most significant. As the principal cation in extracellular fluid, sodium plays a vital role in maintaining fluid balance, enabling nerve impulse transmission, and facilitating muscle contraction.(3) Sweat is hypotonic relative to plasma, but it contains a substantial amount of sodium, and the concentration is highly individual, varying from as little as 200 mg/L (approx. 10 mM) to as much as 2000 mg/L (approx. 90 mM). Failure to adequately replace these sodium losses while consuming large volumes of water can lead to a dangerous dilution of blood sodium concentration, a condition known as hyponatremia, which can cause symptoms ranging from nausea and cognitive impairment to seizures and, in severe cases, death. The importance of maintaining sodium balance is underscored by evidence showing that athletes who effectively replaced their individual sodium losses performed significantly better; for instance, one study found that such athletes completed a middle-distance triathlon an average of 26 min faster. This highlights a critical gap: generic hydration guidelines are insufficient, and there is a pressing need for personalized strategies based on real-time physiological data. The goal is not merely "hydration" but the maintenance of a dynamic state of optimal fluid and electrolyte balance, or euhydration. A real-time monitoring system enables a physiological feedback loop where sodium loss is detected and can be precisely replenished, allowing for the active management of an individual's physiological state during exertion.

Traditional methods for assessing hydration status are ill-suited for this purpose. Clinical "gold standard" techniques, such as measuring plasma osmolality, are invasive, costly, time-consuming, and confined to laboratory settings, making them entirely impractical for in-field monitoring.(4) While a new generation of consumer-grade smart hydration devices has emerged, they often suffer from significant practical limitations, including inconsistent precision, cumbersome calibration procedures requiring multiday baselines, and high sensitivity to sensor-skin contact, all of which compromise their reliability for guiding in-activity decisions. The primary barrier to solving this long-standing physiological challenge has not been a lack of understanding, but a lack of appropriate technology.

Wearable biosensors that analyze sweat offer a promising noninvasive solution. Sweat is an easily accessible biofluid rich in analytes that provide a window into an individual's health and physiological status.(5) Recent advancements in skin-interfaced electrochemical sensors have enabled the continuous, real-time analysis of sweat composition at the point of generation, mitigating historical challenges of sample evaporation and contamination. Among the various electrochemical techniques, potentiometric ion-selective electrodes (ISEs) are particularly advantageous for wearable applications owing to their high performance, portability, low cost,

and operational simplicity. The development of such sensors is a direct application of modern materials science to provide a technological solution to a well-defined physiological need. A key determinant of practical performance in wearable solid-contact ISEs is the stability of ion-to-electron transduction at the membrane/electrode interface,[6] where insufficient interfacial capacitance and the formation of parasitic water layers can manifest as potential drift and slow response. Carbon nanomaterials and conducting polymers are widely used to engineer this interface, but their processing and long-duration stability can differ substantially. We selected multiwalled carbon nanotubes (MWCNTs) because their high aspect ratio enables a percolating conductive network at low loadings, providing efficient capacitive transduction and a mechanically robust interfacial scaffold. Mechanistic studies have shown that CNT-based contacts can yield well-defined transduction behavior in solid-contact ISEs.[1] The determination of venlafaxine HCl is based on a comparison study between different ion-to-electron transduction materials, such as MWCNTs. Graphene-based contacts can also deliver high capacitance and excellent stability in ISE formats, but achieving reproducible performance can be sensitive to sheet restacking and interfacial morphology, which becomes particularly relevant for solution-cast layers on flexible printed substrates.[7] Conducting polymers such as PEDOT:PSS are attractive solid contacts, yet reports have documented pronounced equilibration-associated potential drift and hydration-related effects that can complicate stable, long-duration measurements if not carefully engineered.[8] We report the fabrication, comprehensive characterization, and validation of a flexible, screen-printed potentiometric biosensor for the real-time monitoring of sodium ion concentration in sweat. The novelty of this work lies in the systematic, controlled evaluation of embedding MWCNTs directly into a conventional PVC-based ion-selective membrane (ISM) as an integrated transduction strategy, benchmarked against an otherwise identical baseline membrane, to quantify how nanotube loading governs sensitivity, response time, and potential stability under mechanically relevant conditions.

2. Materials and Methods

2.1 Reagents and materials

High-molecular-weight PVC, the plasticizer bis(2-ethylhexyl) sebacate (DOS), sodium ionophore X (4,13-didecyl-1,7,10,16-tetraoxa-4,13-diazacyclooctadecane), and the anionic additive sodium tetrakis[3,5-bis(trifluoromethyl)phenyl]borate (Na-TFPB) were purchased from Sigma-Aldrich (St. Louis, MO, USA). Anhydrous tetrahydrofuran (THF, ≥99.9%) was also sourced from Sigma-Aldrich and used as the solvent for membrane preparation. MWCNTs (>95% carbon basis, 50–90 nm diameter, 5–20 μm length) were procured from Merck KGaA (Darmstadt, Germany). Flexible polyethylene terephthalate (PET) sheets (0.125 mm thickness, Melinex ST504, DuPont Teijin Films) served as the sensor substrate. Screen-printable conductive carbon ink (Loctite EDAG 423SS) was obtained from Henkel (Düsseldorf, Germany), and Ag/AgCl ink (113-09, 82/18 Ag:AgCl ratio) was sourced from Creative Materials (Ayer, MA, USA). A dielectric insulation ink was used to define the electrode areas. All salts for preparing standard solutions and artificial sweat, including sodium chloride (NaCl), potassium chloride (KCl),

ammonium chloride (NH_4Cl), calcium chloride ($CaCl_2$), magnesium sulfate ($MgSO_4$), urea, and lactic acid, were of analytical grade and purchased from Sigma-Aldrich.

2.2 Fabrication of flexible electrode platform

The three-electrode sensor platform was fabricated on a flexible PET substrate using a semi-automatic screen printer (LS-150TV, Newlong Seimitsu Kogyo Co., Ltd., Japan). Prior to printing, the PET substrates were cleaned by sonication in isopropyl alcohol and DI water for 15 min each, followed by drying under a stream of nitrogen gas. First, the conductive tracks and electrode contact pads were screen-printed using Ag/AgCl ink. Subsequently, a layer of carbon ink was printed over the Ag/AgCl layer to define a circular working electrode (WE) with a diameter of 4 mm and a counter electrode (CE). The underlying Ag/AgCl layer at the reference electrode (RE) site was left exposed to serve as the pseudo-RE.[9] Finally, a dielectric insulation layer was printed over the conductive tracks to precisely define the active sensing areas of the three electrodes and to passivate the interconnects. After each printing step, the ink was cured in a convection oven at 120 °C for 20 min to ensure complete solvent evaporation, strong adhesion to the substrate, and stable electrical properties.[10] Because screen-printed layer thickness can exhibit batch-to-batch dispersion even under semi-automated conditions, we emphasize that all printing and curing parameters were held constant within a batch to maximize reproducibility.

2.3 Synthesis and deposition of ISMs

Three distinct ISM cocktails were prepared to systematically evaluate the effect of MWCNT loading on sensor performance, with their compositions detailed in Table 1. The formulation of the baseline membrane was adapted from optimized ratios reported in the literature to ensure a robust starting point for comparison.[11] For the nanocomposite membranes (ISM-MWCNT-0.5% and ISM-MWCNT-1.0%), the specified mass of MWCNTs was first dispersed in 1 mL of THF using a probe ultrasonicator (Branson Sonifier 450) for 30 min at 40% amplitude in an ice bath to prevent overheating and ensure a homogeneous dispersion.[12] Following dispersion, the remaining components were added to the MWCNT-THF suspension. The mixtures were then stirred in sealed vials for approximately 4 h until all components were fully dissolved, yielding black, viscous solutions. For the baseline membrane (ISM-base), all components were simply dissolved in THF with magnetic stirring. A precise volume of 8 μL of each respective ISM

Table 1
Formulations of ISMs.

Component	ISM-base (wt%)	ISM-MWCNT-0.5% (wt%)	ISM-MWCNT-1.0% (wt%)
PVC	33.0	32.75	32.5
DOS	65.0	64.75	64.5
Sodium ionophore X	1.5	1.5	1.5
Na-TFPB	0.5	0.5	0.5
MWCNTs	0.0	0.5	1.0
Total	100.0	100.0	100.0

cocktail was then carefully drop-cast onto the surface of a carbon WE. The coated electrodes were left to dry at ambient room temperature for 24 h in a dust-free environment. This slow solvent evaporation process facilitates the formation of a uniform, nonporous, and mechanically stable membrane layer essential for reliable potentiometric sensing.[13] Since the ISM is applied by fixed-volume drop-casting (rather than screen printing), the dominant practical contributors to membrane thickness variability are the dispensed volume and drying environment; accordingly, the ISM volume was fixed for all sensors and drying was performed under consistent ambient conditions to minimize sensor-to-sensor variation. From a mechanistic standpoint, membrane thickness and ion-transport length scales can affect potentiometric dynamics through membrane resistance and diffusion-limited processes.

2.4 Electrochemical performance assessment

All potentiometric measurements were conducted at room temperature using a Keithley 2636B high-impedance multichannel sourcemeter.[14] The fabricated three-electrode sensors were connected to the sourcemeter, and the open-circuit potential (OCP) between the WE and the RE was recorded. For calibration, sensors were sequentially immersed in standard NaCl solutions with concentrations ranging from 10^{-5} M to 1.0 M, prepared in a 0.01 M Tris-HCl buffer (pH 7.4). The steady-state potential at each concentration was recorded, and calibration curves were generated by plotting the potential versus the logarithm of Na^+ activity. The dynamic response time was determined by measuring the time required for the sensor to reach 95% of the final steady potential upon switching from a 10 to a 100 mM NaCl solution.[15] Long-term stability was evaluated by continuously monitoring the sensor's potential in a 50 mM NaCl solution for 8 h, and the potential drift was calculated in mV/h.[16] The selectivity of the potentiometric sweat sodium sensor was evaluated using the fixed interference method (FIM) for potentiometric selectivity coefficients. The potential was recorded in a 50 mM NaCl background (within the commonly reported eccrine sweat [Na^+] window under exercise/heat stress) before and after spiking the following physiologically relevant interferents at concentrations representative of human sweat: KCl (10 mM), NH_4Cl (1 mM), $CaCl_2$ (1 mM), and a Mg^{2+} source (0.1 mM). These concentrations were selected to match the reported orders of magnitude in eccrine sweat (Na^+ typically ~10–90 mM; K^+ commonly in the low-to-upper single-digit mM range but variable; NH_4^+ often ~1–8 mM; Ca^{2+} ~0.2–2.0 mM; Mg^{2+} ~0.02–0.40 mM). The potentiometric selectivity coefficients were then calculated using the standard FIM formalism.

2.5 Mechanical integrity testing

The mechanical robustness of the flexible sensors was evaluated to ensure their suitability for on-body applications. Cyclic bending tests were performed using a custom-built motorized stage that repeatedly bent the sensor around a 1-cm-diameter mandrel for 5000 cycles at a frequency of 1 Hz. The sensor's calibration curve was measured before the test and after every 1000 cycles to monitor any degradation in performance.[17] Similarly, cyclic stretching tests were conducted

by uniaxially stretching the sensor to 20% strain for 2000 cycles. The potential response in a fixed 50 mM NaCl solution was recorded throughout the test to assess signal stability under mechanical strain.[18]

2.6 On-body validation protocol

The on-body validation study was conducted with the approval of the Institutional Review Board (IRB #2024-045), and written informed consent was obtained from ten healthy volunteers (5 male, 5 female, age 25 ± 4 years). The optimized sensor (ISM-MWCNT-1.0%) was integrated into a soft, adhesive patch and affixed to the subject's clean, dry forearm. Subjects performed a 60 min cycling protocol on a stationary ergometer in a climate-controlled chamber (27 °C, 45% relative humidity).[19] The sensor's potential was recorded continuously and transmitted wirelessly via a custom-built Bluetooth module to a laptop for real-time data logging.[20] To address practical wearable considerations, we now provide a concise hardware description and operating settings of the module (Table 2).

For validation, sweat samples were collected concurrently from an adjacent area on the same arm using a Macroduct® Sweat Collection System (Wescor Inc.). Discrete sweat samples were collected every 15 min. The sodium concentration of these collected samples was analyzed using a Dionex ICS-6000 ion chromatography (IC) system; this served as the gold-standard reference method.[21] The data from the wearable sensor were then correlated with the IC results to assess the on-body accuracy of the device.

3. Results and Discussion

3.1 Structural and morphological characterization of the sensor platform

The surface morphology of the individual electrode components and ISMs was investigated by scanning electron microscopy (SEM). Representative images are shown in Fig. 1. The bare screen-printed carbon WE [Fig. 1(a)] exhibits a porous microstructure composed of

Table 2.
Key specifications of the Bluetooth data acquisition module.

Parameter	Specification
Wireless communication protocol	Bluetooth Low Energy (BLE) 5.0
Microcontroller unit (MCU)	32-bit ARM Cortex-M4F (low-power SoC)
ADC resolution	16-bit (effective number of bits: 14.5)
Input impedance	> 1 TΩ (10^{12} Ω)
Voltage measurement range	−500 mV to +500 mV
Sampling rate	1 Hz (1 sample/s)
Data transmission interval	1 s (real-time update)
Power supply	3.7 V, 150 mAh lithium-polymer (Li-Po) battery
Operational current consumption	~4.5 mA (average during transmission)
Estimated continuous runtime	> 24 h
Physical dimensions	20 × 15 × 4 mm^3

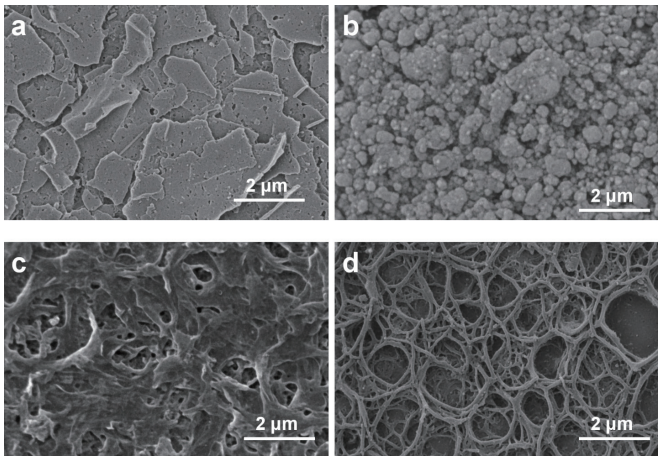

Fig. 1. SEM images of sensor components. (a) Surface of the bare screen-printed carbon WE. (b) Surface of the screen-printed Ag/AgCl RE. (c) Surface of the ISM-base membrane cast on the WE. (d) Surface of the ISM-MWCNT-1.0% membrane, showing a textured morphology due to the embedded MWCNT network.

interconnected graphite flakes and carbon black particles, which provides a large surface area for subsequent membrane deposition. The screen-printed Ag/AgCl RE [(Fig. 1(b)] displays a dense, particulate structure consisting of Ag and AgCl microparticles embedded within a polymer binder. After drop-casting, the baseline ISM-base membrane forms a smooth and uniform film covering the underlying carbon electrode [Fig. 1(c)], which is characteristic of a solvent-cast PVC film. In stark contrast, the surface of the ISM-MWCNT-1.0% membrane [Fig. 1(d)] reveals a significantly more textured and nanostructured morphology. The embedded MWCNTs create a web-like network within the polymer matrix, increasing the surface roughness and porosity. This structural modification is hypothesized to be a key factor in enhancing the sensor's electrochemical performance by increasing the interfacial area between the membrane and the solid contact.

3.2 Physicochemical and compositional analysis

The chemical composition of the membranes was confirmed by FTIR-ATR spectroscopy. Figure 2 displays the overlaid spectra of the raw components and the final ISM-base membrane. The spectrum of pure PVC shows its characteristic peaks, including the strong C–Cl stretching vibration at 610 cm^{-1} and the C–H bending modes at around 1430 cm^{-1}. The plasticizer DOS is identified by its prominent C=O ester stretching peak at 1720 cm^{-1} and C–H stretching peaks at around 2880–2970 cm^{-1}. The spectrum of the final ISM-base membrane is a composite of its constituents, clearly showing the characteristic peaks from both PVC and DOS. The successful incorporation of the sodium ionophore X is also confirmed by the presence of its characteristic ether C–O–C stretching vibrations at around 1160 cm^{-1}. The spectrum for the ISM-MWCNT-1.0% membrane (not shown) was virtually identical to that of the ISM-base membrane, as carbon nanotubes are largely inactive in the mid-infrared region and do not obscure the polymer matrix signals.

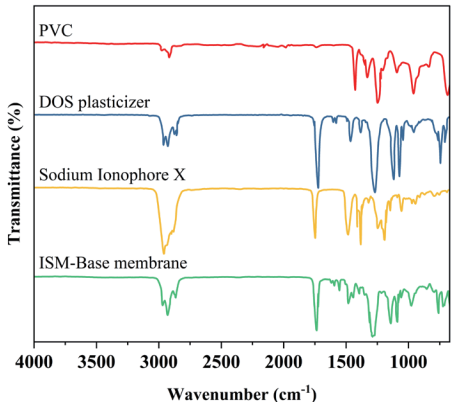

Fig. 2. (Color online) FTIR spectra of the pure PVC polymer, DOS plasticizer, sodium ionophore X, and final cast ISM-base membrane.

X-ray diffraction (XRD) analysis was performed to investigate the crystalline structure of the screen-printed layers and the amorphous nature of the polymer membrane. As shown in Fig. 3, the XRD pattern of the final sensor reveals several distinct features. The broad hump centered around $2\theta = 20°$ is attributed to the amorphous PET substrate and the PVC-based ISM. Superimposed on this amorphous background are sharp diffraction peaks that can be indexed to the crystalline phases of silver (Ag) and silver chloride (AgCl) from the RE ink. The peaks at 2θ values of 38.1, 44.3, and 64.4° correspond to the (111), (200), and (220) planes of face-centered cubic Ag (JCPDS No. 04-0783). The peaks at 27.8, 32.2, and 46.2° correspond to the (111), (200), and (220) planes of crystalline AgCl (JCPDS No. 31-1238).[22] This confirms the successful deposition of the intended crystalline materials for the RE and the amorphous nature of the sensing membrane.[23]

3.3 Electrochemical performance and sensing mechanism

The electrochemical performance of the three sensor types was systematically evaluated, and the key metrics are summarized in Table 3. Figure 4 shows the potentiometric calibration curves for the sensors in response to various concentrations of NaCl. All sensors exhibited a linear response over a wide concentration range. However, a clear trend of performance enhancement with increasing MWCNT content was observed. The ISM-base sensor displayed a sub-Nernstian sensitivity of 45.5 ± 1.2 mV/decade. The sensitivity improved to 52.1 ± 0.9 mV/decade for the ISM-MWCNT-0.5% sensor, and the ISM-MWCNT-1.0% sensor achieved a near-Nernstian response of 58.2 ± 0.7 mV/decade, which is close to the theoretical value of 59.16 mV/decade at 25 °C. We further investigated a higher loading of 1.5 wt% to determine the upper limit of optimization. However, at this concentration, the dispersion quality deteriorated significantly, with visible MWCNT agglomeration disrupting the homogeneity of the membrane.[24] This aggregation led to increased signal noise and potential drift (0.8 ± 0.2 mV/h) due to the formation of aqueous pockets at the interface, and the resulting membranes exhibited reduced mechanical flexibility, showing susceptibility to micro-cracking during bending tests. Consequently, 1.0 wt% was identified as the optimal percolation threshold, balancing efficient charge transduction

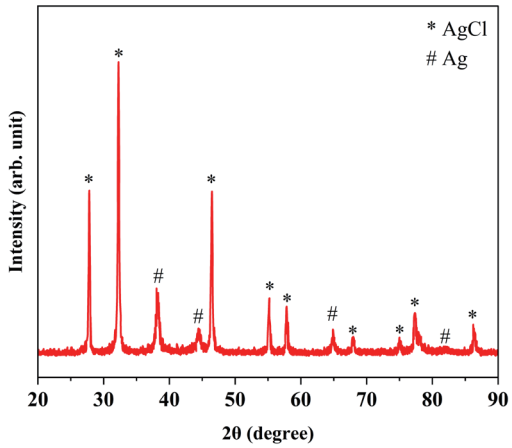

Fig. 3. (Color online) XRD pattern of the fully fabricated sensor on a PET substrate.

Table 3
Summary of electrochemical performance metrics for the fabricated sodium sensors.

Performance metric	ISM-base	ISM-MWCNT-0.5%	ISM-MWCNT-1.0%
Sensitivity (mV/decade)	45.5 ± 1.2	52.1 ± 0.9	58.2 ± 0.7
Linear range (M)	1×10^{-3}–1.0	5×10^{-4}–1.0	1×10^{-4}–1.0
Limit of detection (M)	8.5×10^{-4}	3.2×10^{-4}	9.1×10^{-5}
Response time (t_{95}, s)	28 ± 3	15 ± 2	< 10
Potential drift (mV/h)	1.2 ± 0.3	0.4 ± 0.1	0.1 ± 0.04

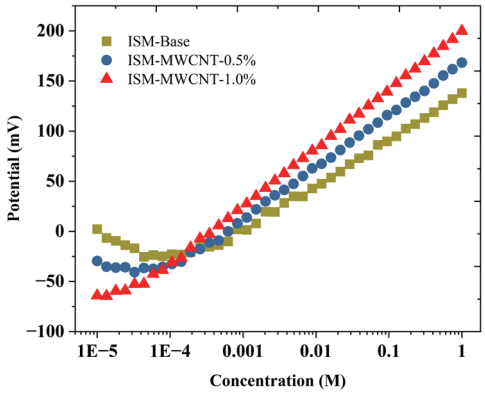

Fig. 4. (Color online) Potentiometric calibration curves for the ISM-base, ISM-MWCNT-0.5%, and ISM-MWCNT-1.0% sensors in standard NaCl solutions (10^{-5} to 1.0 M).

with membrane structural integrity. This sensor also demonstrated the widest linear range, from 1×10^{-4} M to 1.0 M, and the lowest limit of detection (9.1×10^{-5} M), covering the entire physiological range of sodium in sweat.[25]

This performance enhancement is attributed to the multifaceted role of the MWCNTs. The nanotubes form a percolating conductive network at the interface between the insulating ISM and the underlying carbon electrode, acting as an efficient solid-contact ion-to-electron

transducer. This network lowers the interfacial impedance and facilitates more stable and rapid charge transfer. Furthermore, the significantly increased surface area, as confirmed by BET analysis, provides more active sites for the ion-exchange equilibrium between the sample and the ionophore-doped membrane, leading to a larger and more stable potential signal.[24] The rigid nanotube network may also mechanically stabilize the interface, inhibiting the formation of an unstable water layer, which is a common cause of potential drift in solid-contact ISEs.

The dynamic response of the sensors is shown in Fig. 5. When rapidly transferred between 10 and 100 mM NaCl solutions, the optimized ISM-MWCNT-1.0% sensor reached a stable potential in less than 10 s. In contrast, the ISM-base sensor exhibited a significantly slower response, with t_{95} of approximately 28 s. This rapid response is critical for wearable applications, where the sensor must be able to track dynamic changes in sweat electrolyte concentrations in real time.[15] The enhanced charge transfer kinetics and ion transport within the porous nanocomposite membrane are responsible for this improvement.

Long-term signal stability is another crucial parameter for continuous monitoring. Figure 6(a) illustrates the potential drift of the sensors over an 8 h period in a 50 mM NaCl solution. The ISM-base sensor showed a considerable drift of 1.2 mV/h. The incorporation of MWCNTs markedly improved stability, with the ISM-MWCNT-1.0% sensor demonstrating an exceptionally low drift of only 0.1 mV/h. This high level of stability is attributed to the well-defined and robust interface provided by the MWCNT solid contact, which minimizes parasitic electrochemical reactions and water layer formation.

The sensor's selectivity against common sweat interferents was evaluated using the FIM (Figs. 6(b) and 6(c), and Table 4). To ensure physiological relevance, the FIM was conducted in 50 mM NaCl and the interferents were introduced at concentrations consistent with the reported eccrine sweat composition during exercise/heat exposure (K^+ 10 mM, NH_4^+ 1 mM, Ca^{2+} 1 mM, Mg^{2+} 0.1 mM). The ISM-MWCNT-1.0% sensor exhibited excellent selectivity for Na^+ over K^+, NH_4^+, Ca^{2+}, and Mg^{2+}. Notably, even when considering the upper ends of commonly reported sweat ranges, the Nicolsky–Eisenman selectivity coefficients in Table 4 imply negligible Na^+-

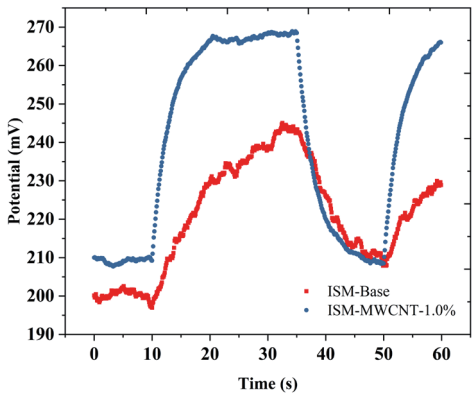

Fig. 5. (Color online) Dynamic response times of the ISM-base and ISM-MWCNT-1.0% sensors when alternating between 10 and 100 mM NaCl solutions.

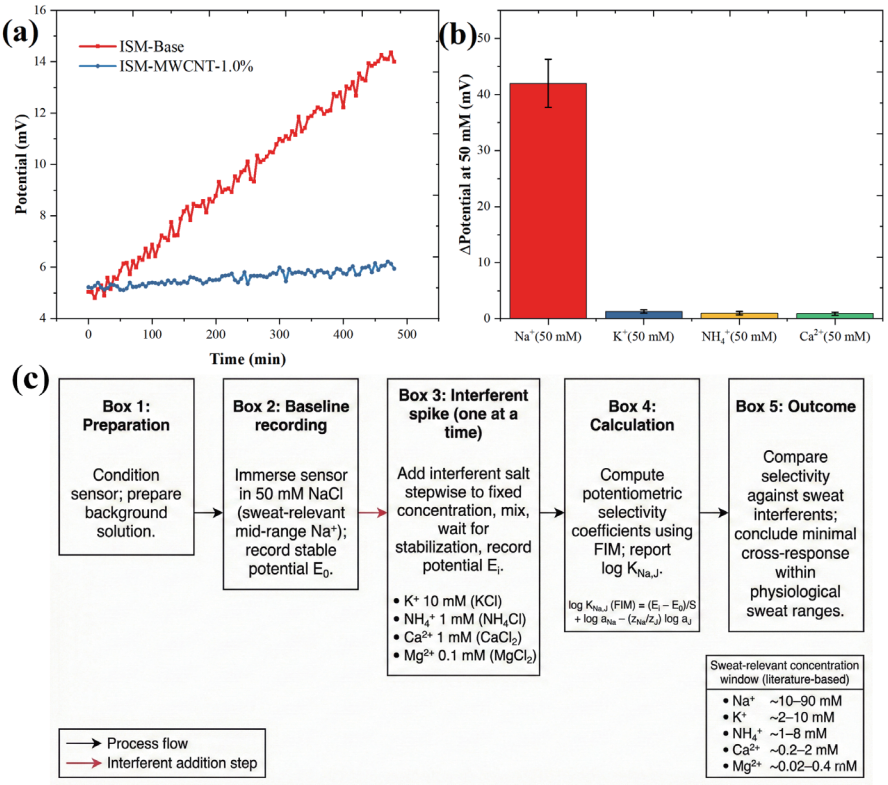

Fig. 6. (Color online) (a) Long-term stability test showing the potential drift of the ISM-base and ISM-MWCNT-1.0% sensors over 8 h of continuous measurement in a 50 mM NaCl solution. (b) Bar chart showing the potentiometric response of the optimized ISM-MWCNT-1.0% sensor to 50 mM solutions of the primary ion (Na^+) and major interfering ions (K^+, NH_4^+, Ca^{2+}). (c) Workflow schematic of the FIM selectivity protocol used in this study, including the NaCl background (50 mM) and sweat-relevant interferent concentrations (K^+ 10 mM, NH_4^+ 1 mM, Ca^{2+} 1 mM, Mg^{2+} 0.1 mM) with literature-based physiological concentration windows.

Table 4
Potentiometric selectivity coefficients of the optimized sensor (ISM-MWCNT-1.0%).

Interfering ion (j)	Concentration (M)	$\log K_{Na,j}^{pot}$
K^+	1×10^{-2}	−2.5
NH_4^+	1×10^{-3}	−2.8
Ca^{2+}	1×10^{-3}	−3.1
Mg^{2+}	1×10^{-4}	−3.4

equivalent interference (for example, at NH_4^+ = 8 mM, Ca^{2+} = 2 mM, and Mg^{2+} = 0.4 mM, the corresponding Na^+-equivalent contributions remain on the order of <0.04 mM), which is practically insignificant relative to the typical sweat [Na^+] range (tens of mM). These results support robust Na^+ specificity in real sweat matrices without meaningful cross-response from major inorganic constituents.

3.4 Mechanical robustness for wearable applications

For a sensor to be practical in a wearable format, it must withstand the mechanical stresses associated with body movement. The mechanical integrity of the optimized ISM-MWCNT-1.0% sensor was assessed through rigorous bending and stretching tests. Figure 7(a) shows the effect of repeated bending on the sensor's sensitivity. Even after 5000 bending cycles around a 1-cm-radius mandrel, the Nernstian slope of the sensor remained stable at 57.9 ± 0.8 mV/decade, showing less than a 5% deviation from its initial value. This result demonstrates the excellent adhesion between the screen-printed layers and the flexible PET substrate, as well as the intrinsic flexibility of the PVC-based membrane.[18] Similarly, the sensor's performance under tensile strain was evaluated. Figure 7(b) shows plots of the relative change in the sensor's potential while being subjected to 2,000 stretching cycles at 20% strain. The potential signal exhibited minimal fluctuation, with a standard deviation of less than 2 mV from the baseline. A photograph of the actual cyclic bending configuration used to generate these data is provided in Fig. 7(c).

3.5 On-body validation and application for personalized hydration

Following extensive laboratory characterization, the optimized ISM-MWCNT-1.0% sensor was tested on human subjects to validate its performance in a real-world application. Figure 8(a) displays the real-time sweat sodium concentration profile from a representative subject during a

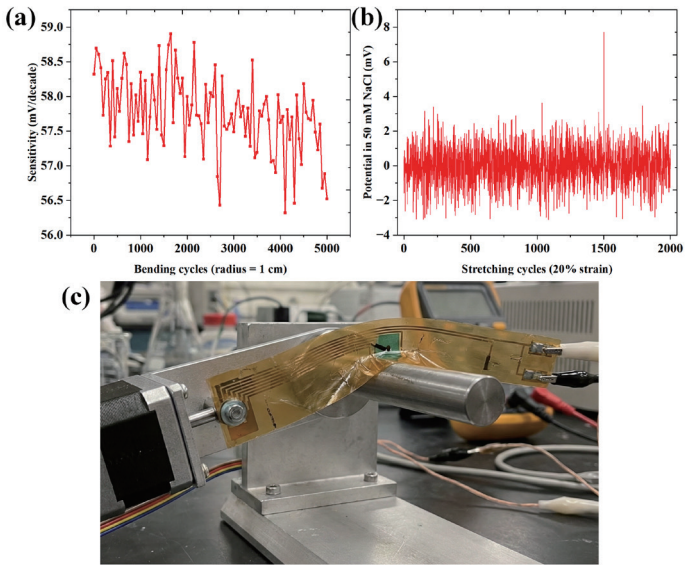

Fig. 7. (Color online) (a) Results of the cyclic bending test on the ISM-MWCNT-1.0% sensor. The plot shows the Nernstian sensitivity of the sensor as a function of the number of bending cycles. (b) Results of the cyclic stretching test on the ISM-MWCNT-1.0% sensor. The plot shows the stability of the potential reading in a 50 mM NaCl solution over 2000 stretching cycles to 20% strain. (c) b) Photograph of the cyclic bending apparatus used in this study, showing the sensor positioned on the mandrel during repeated flexing (5000 cycles).

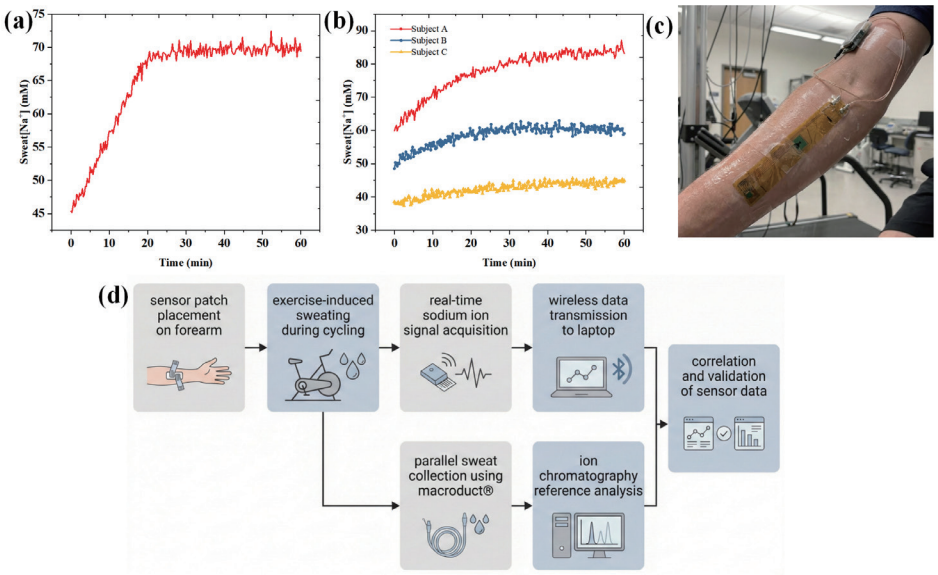

Fig. 8. (Color online) (a) Real-time on-body sweat sodium concentration measured by the wearable sensor from a representative subject during a 60 min cycling exercise. (b) Real-time sweat sodium concentration profiles from three different subjects during the same 60 min cycling protocol, illustrating significant interindividual variability. (c) Photograph of the wearable sensor integrated into an adhesive patch and attached to a subject's forearm during stationary cycling, demonstrating practical adhesion and on-skin deployment during motion. (d) Block-style workflow diagram of the on-body trial and validation procedure, including patch placement, real-time wireless logging, parallel sweat collection using Macroduct®, and IC reference analysis.

60 min cycling exercise. The sensor successfully captured the dynamic changes in sweat composition, showing an initial increase in [Na^+] from 45 to 68 mM during the first 20 min, which corresponds to an increasing sweat rate, followed by a gradual stabilization at around 70 mM for the remainder of the exercise. This dynamic profile provides valuable insight into the individual's physiological response to the exercise load. The on-body tests also highlighted the significant interindividual variability in sweat sodium loss, reinforcing the need for personalized monitoring. As shown in Fig. 8(b), the sweat sodium concentration profiles varied substantially among three different subjects performing the same exercise protocol. Subject A exhibited a high and rising [Na^+] ("salty sweater"), while Subject C maintained a much lower and more stable [Na^+]. This variability confirms that the sensor's wide dynamic range, established during laboratory calibration, is not merely an academic parameter but is essential for the device to be universally applicable across a diverse population.

Figure 8(c) now shows the sensor patch adhered to the subject's forearm during the stationary ergometer protocol. In addition, Fig. 8(d) provides a concise workflow diagram summarizing the on-body measurement, parallel reference sampling, and data handling used to generate the human-trial results. This dynamic profile provides valuable insight into the individual's physiological response to the exercise load.

To quantitatively assess the accuracy of the wearable sensor, its measurements were compared against the gold-standard IC method. Figure 9(a) shows a correlation plot of the [Na^+] values obtained from the wearable sensor versus those from the IC analysis of concurrently

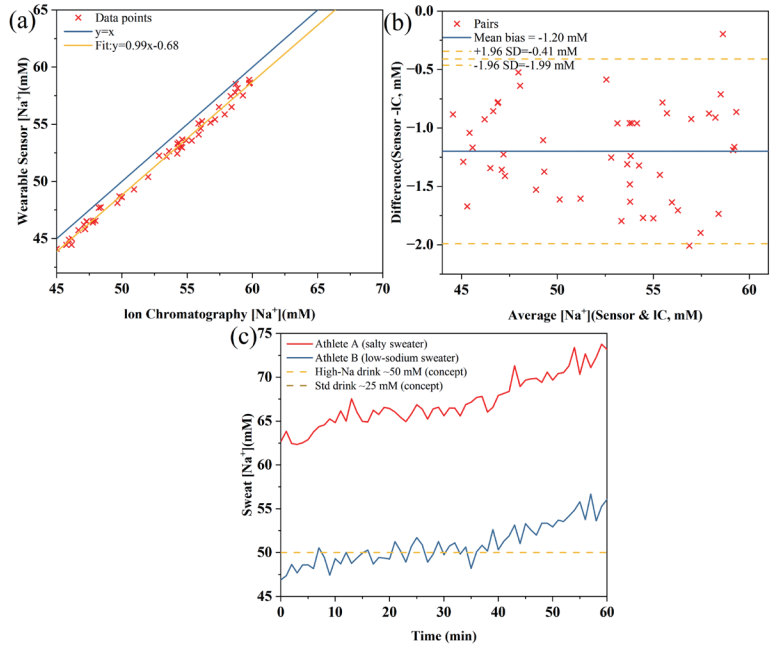

Fig. 9. (Color online) (a) Correlation plot of sweat sodium concentrations measured by the wearable sensor versus the gold-standard IC method. Data points were collected from 10 subjects at 15 min intervals during exercise. (b) Bland–Altman plot of the sweat sodium concentrations obtained from the wearable sensor and the IC reference method. (c) Conceptual illustration of personalized hydration strategies based on real-time sweat sodium data from two athletes with different sweat profiles ("salty sweater" vs "low-sodium sweater").

collected sweat samples. The data show an excellent linear correlation between the two methods, with a Pearson correlation coefficient (R^2) of 0.985. The slope of the regression line is 0.99, and the y-intercept is close to zero, indicating a strong one-to-one correspondence with minimal systematic bias.[25]

A Bland–Altman analysis was also performed to further evaluate the agreement between the two methods [Fig. 9(b)]. The plot shows that 95% of the data points fall within the limits of agreement (±1.96 standard deviations), with a small mean bias of −1.2 mM. This indicates that the wearable sensor slightly underestimates the sodium concentration compared with IC, but the difference is not statistically significant and is well within the acceptable range for physiological monitoring, confirming the sensor's high degree of accuracy for on-body applications.

The utility of this real-time data is in its application to personalized hydration strategies. Figure 9(c) illustrates how the sensor data could be used to differentiate between athletes with different sweating profiles. Athlete A, a "salty sweater" with a high sweat [Na^+], would require a hydration fluid with a higher electrolyte concentration to adequately replace losses. In contrast, Athlete B, with a lower sweat [Na^+], could maintain electrolyte balance with a standard or lower-concentration sports drink. By providing this individualized, real-time feedback, the sensor enables athletes to move beyond generic guidelines and implement a hydration strategy tailored to their unique physiology, thereby optimizing performance and safety.

4. Conclusions

In this work, a wearable sweat sodium ion biosensor based on an ISM and a MWCNT-modified transduction layer was developed and validated for personalized hydration monitoring under exercise-induced heat stress. The sensor demonstrated high sensitivity, a wide linear response range covering physiologically relevant sweat sodium concentrations, strong selectivity against common interfering ions, and robust operational stability. Importantly, on-body human trials confirmed the capability of the device to continuously track dynamic sweat [Na^+] profiles during exercise and to resolve pronounced interindividual differences. A key outcome of the human validation is the clear identification of a 'salty sweater' phenotype, characterized by consistently elevated and, in some cases, rising sweat sodium concentrations under identical exercise conditions. This phenotype represents the scenario in which real-time electrolyte monitoring provides the greatest practical value. The continuous detection of sustained high sweat [Na^+] enables a shift from generic hydration advice toward actionable, individualized guidance, such as triggering a real-time prompt to initiate electrolyte intake when sodium losses are likely to be substantial. In contrast, individuals exhibiting lower and more stable sweat [Na^+] profiles may not require the same frequency or concentration of electrolyte supplementation. While whole-body sodium loss ultimately depends on both sweat sodium concentration and sweat rate, the present results demonstrate that real-time sweat [Na^+] sensing alone is sufficient to identify high-risk electrolyte-loss phenotypes and to support decision-making frameworks when combined with established sweat-rate estimation approaches. Overall, this study establishes a physiologically grounded and practically relevant foundation for wearable, sodium-informed hydration strategies. Future work will focus on integrating this sensor into multiplexed sweat-analysis platforms and implementing intuitive alert logic within mobile health interfaces to further enhance real-time, personalized hydration management.

References

1 H. M. Hashem and A. B. Abdallah: Sci. Rep. **14** (2024) 5405. https://doi.org/10.1038/s41598-024-55729-8
2 L. G. Ioannou, J. Foster, N. B. Morris, J. F. Piil, G. Havenith, I. B. Mekjavic, G. P. Kenny, L. Nybo, and A. D. Flouris: Temperature **9** (2022) 67. https://doi.org/10.1080/23328940.2022.2030634
3 A. Hunt, A. Essa, and R. Macnab: Anaesth. Intensive Care Med. **25** (2024) 332. https://doi.org/10.1016/j.mpaic.2024.03.007
4 S. Cheraghi, M. Dasar, and M. Taher: J. Nanostruct. Chem. **15** (2025) 152510. https://doi.org/10.57647/jnsc.2025.1503.10
5 A. Erdem, E. Eksin, H. Senturk, E. Yildiz, and M. Maral: TrAC Trends Anal. Chem. **171** (2024) 117510. https://doi.org/10.1016/j.trac.2023.117510
6 N. Zare, H. Karimi-Maleh, Z. Zhang, L. Fu, J. Rouhi, N. Zhong, Y. Wen, and M. Ghalkhani: Carbon Lett. **35** (2025) 1691. https://doi.org/10.1007/s42823-025-00887-6
7 F. Li, J. Ye, M. Zhou, S. Gan, Q. Zhang, D. Han, and L. Niu: Analyst **137** (2012) 618. https://doi.org/10.1039/C1AN15705A
8 M. Guzinski, J. M. Jarvis, F. Perez, B. D. Pendley, E. Lindner, R. De Marco, G. A. Crespo, R. G. Acres, R. Walker, and J. Bishop: Anal. Chem. **89** (2017) 3508. https://doi.org/10.1021/acs.analchem.6b04625
9 L. R. Stromberg, J. A. Hondred, D. Sanborn, D. Mendivelso-Perez, S. Ramesh, I. V. Rivero, J. Kogot, E. Smith, C. Gomes, and J. C. Claussen: Microchimica Acta **186** (2019) 533.
10 M. Sophocleous and J. K. Atkinson: Sens. Actuators, A **267** (2017) 106.
11 J.-L. Lin and H.-Y. Hsu: Sensors **10** (2010) 1798. https://doi.org/10.3390/s100301798

12 F.-H. Wang, S.-W. Huang, C.-F. Yang, and K.-W. Min: Sensors **25** (2025) 3650. https://doi.org/10.3390/s25123650
13 M. Pięk, A. Wojciechowska, K. Fendrych, R. Piech, and B. Paczosa-Bator: Ionics **25** (2019) 2311.
14 A. Zörner, S. Oertel, B. Schmitz, N. Lang, M. P. M. Jank, and L. Frey: Proc. 10th Int. Joint Conf. Biomedical Engineering Systems and Technologies (2017). https://doi.org/10.5220/0006296400810087
15 A. M. Noor, M. S. Al Farisi, M. Mazalan, N. F. A. Ibrahim, A. A. Wahab, Z. Zakaria, N. I. Rusli, N. Sabani, and A. A. Manaf: Sensors **25** (2025) 3467. https://doi.org/10.3390/s25113467
16 D. Y. Kim, M. S. Reza, A. A. Samad, Z. Islam, J. W. Go, and J. Y. Park: Micro Nano Syst. Lett. **13** (2025) 15.
17 A. K. Persons, J. E. Ball, C. Freeman, D. M. Macias, C. L. Simpson, B. K. Smith, and R. F. Burch V: Materials **14** (2021) 4070.
18 M. Parrilla, R. Cánovas, I. Jeerapan, F. J. Andrade, and J. Wang: Adv. Healthcare Mater. **5** (2016) 996. https://doi.org/10.1002/adhm.201600092
19 C. Lafaye, M. Rovira, S. Demuru, S. Wang, J. Kim, B. P. Kunnel, C. Besson, C. Fernandez-Sanchez, F. Serra-Graells, J. M. Margarit-Taule, J. Aymerich, J. Cuenca, I. Kiselev, V. Gremeaux, M. Saubade, C. Jimenez-Jorquera, D. Briand, and S.-C. Liu: 2022 IEEE Biomedical Circuits and Systems Conf. (BioCAS) (2022). https://doi.org/10.1109/BioCAS54905.2022.9948565
20 N. Brasier, J. Wang, W. Gao, J. R. Sempionatto, C. Dincer, H. C. Ates, F. Güder, S. Olenik, I. Schauwecker, D. Schaffarczyk, E. Vayena, N. Ritz, M. Weisser, S. Mtenga, R. Ghaffari, J. A. Rogers, and J. Goldhahn: Nature **636** (2024) 57.
21 H. Liu, Z. Gu, Y. Liu, X. Xiao, and G. Xiu: Biosensors **12** (2022) 229. https://doi.org/10.3390/bios12040229
22 C. Han, L. Ge, C. Chen, Y. Li, Z. Zhao, X. Xiao, Z. Li, and J. Zhang: J. Mater. Chem. A **2** (2014) 12594.
23 M. Parrilla, I. Ortiz-Gomez, R. Canovas, A. Salinas-Castillo, M. Cuartero, and G. A. Crespo: Anal. Chem. **91** (2019) 8644.
24 Z. Wang, A. Alwattar, P. Quayle, J. C. Batchelor, and A. J. Casson: 2022 IEEE Sensors (2022). https://doi.org/10.1109/SENSORS52175.2022.9967139
25 E. D. Goulet, A. Asselin, J. Gosselin, and L. B. Baker: Appl. Physiol. Nutr. Metab. **42** (2017) 861.